Naval Research Laboratory

Washington, DC 20375-5320

Design of a High Power Thermionic Magnicon Amplifier at 11.4 GHz

STEVEN H. GOLD

Beam Physics Branch
Plasma Physics Division

OLEG A. NEZHEVENKO
VIACHESLAV P. YAKOVLEV

OMEGA-P Inc.
New Haven, CT

B. HAFIZI

ICARUS Research
P.O. Box 30780
Bethesda, MD 20824

August 9, 1996

19960821 079

DTIC QUALITY INSPECTED 1

REPORT DOCUMENTATION PAGE

Public reporting burden for this collection of information is estimated to average 1 hour per response, including the time for reviewing instructions, searching existing data sources, gathering and maintaining the data needed, and completing and reviewing the collection of information. Send comments regarding this burden estimate or any other aspect of this collection of information, including suggestions for reducing this burden, to Washington Headquarters Services, Directorate for Information Operations and Reports, 1215 Jefferson Davis Highway, Suite 1204, Arlington, VA 22202-4302, and to the Office of Management and Budget, Paperwork Reduction Project (0704-0188), Washington, DC 20503.

1. AGENCY USE ONLY (Leave Blank)	2. REPORT DATE August 9, 1996	3. REPORT TYPE AND DATES COVERED Interim	
4. TITLE AND SUBTITLE Design of a High Power Thermionic Magnicon Amplifier at 11.4 GHz			**5. FUNDING NUMBERS** JO# 67-5739-0-6
6. AUTHOR(S) Oleg A. Nezhevenko,* Viacheslav P. Yakovlev,* Steven H. Gold and B. Hafizi**			
7. PERFORMING ORGANIZATION NAME(S) AND ADDRESS(ES) Naval Research Laboratory Washington, DC 20375-5320			**8. PERFORMING ORGANIZATION REPORT NUMBER** NRL/MR/6790–96-7857
9. SPONSORING/MONITORING AGENCY NAME(S) AND ADDRESS(ES) Department of Energy Office of Naval Research Washington, DC 20375 Arlington, VA 22217			**10. SPONSORING/MONITORING AGENCY REPORT NUMBER**

11. SUPPLEMENTARY NOTES

*OMEGA-P, Inc. New Haven, CT 06520-2008
**ICARUS Research, P.O. Box 30780, Bethesda, MD 20824

12a. DISTRIBUTION/AVAILABILITY STATEMENT Approved for public release, distribution unlimited.	12b. DISTRIBUTION CODE

13. ABSTRACT (Maximum 200 words)

The Magnicon is a high power, highly efficient microwave amplifier tube for use in powering the next generation of high gradient electron linear accelerators. In this paper, we discuss the design of a thermionic magnicon experiment to produce 50 MW at 11.4 GHz, using a 200 a, 500 kV beam from a thermionic electron gun.

14. SUBJECT TERMS Magnicon Amplifier Thermionic			15. NUMBER OF PAGES 46
			16. PRICE CODE
17. SECURITY CLASSIFICATION OF REPORT UNCLASSIFIED	18. SECURITY CLASSIFICATION OF THIS PAGE UNCLASSIFIED	19. SECURITY CLASSIFICATION OF ABSTRACT UNCLASSIFIED	20. LIMITATION OF ABSTRACT UL

CONTENTS

iii

DESIGN OF A HIGH POWER THERMIONIC MAGNICON AMPLIFIER AT 11.4 GHZ

I. INTRODUCTION

The magnicon [1–3] is a scanning–beam microwave amplifier that is under development as an alternative to klystrons for powering future high gradient electron linear accelerators such as the proposed 0.5 TeV Next Linear Collider (NLC). We have previously published a design study for a frequency–doubling 11.4 GHz magnicon employing a ~200 A, 500 kV, 5.5-mm-diam. electron beam from a plasma cathode [4]. That study led to construction and testing of a single-shot magnicon amplifier experiment on the Long Pulse Accelerator Facility [5] at the Naval Research Laboratory (NRL). This experiment, discussed in Ref. [6], succeeded in demonstrating high power magnicon operation (14 MW at ~10% efficiency) but discovered major limitations to operating the experiment on a single-shot basis employing a typical pulsed-power vacuum (~10^{-5} Torr). A low field saturation problem in the deflection cavities due to plasma formation restricted high power operation to parameters for which the final deflection cavity (the penultimate cavity) was unstable. Thus, true amplifier operation could not be demonstrated, and in addition, the output efficiency was substantially lower than predicted. The conclusion was that demonstration of a high power, high efficiency magnicon amplifier required the transition of the experiment to an ultrahigh vacuum environment using a thermionic electron gun driven by a rep-rated modulator. The Budker Institute of Nuclear Physics

(INP) is presently carrying out thermionic magnicon experiments at 7 GHz. Reference [7] discusses recent results from these experiments. Those results were temporarily constrained by an oversized electron beam (4-mm diameter instead of 3-mm diameter) that was attributed to a mismatch of the beam into the magnetic field, but nevertheless achieved 30 MW at 35% efficiency.

In this paper, we present the results of a design study for a new thermionic magnicon amplifier experiment at NRL. The design has been optimized for the predicted parameters of a new ultrahigh convergence 500 kV, 200 A thermionic electron gun that is being developed by Litton Electron Devices. The new design incorporates a number of circuit improvements that are intended to raise the efficiency while reducing the surface RF electric fields in the magnicon cavities. The design has a predicted efficiency of 58.6% and a maximum surface electric field of 570 kV/cm.

II. THEORETICAL MODELING AND DESIGN PROCEDURE

In order to carry out this investigation, a combination of steady-state and time-dependent magnicon simulation codes was used. Each of these codes can follow an ensemble of electrons in the realistic fields of a sequence of magnicon deflection cavities, followed by an output cavity, and take full account of the effects of nonideal fields in the vicinity of cavity apertures. The time-dependent code can evolve to a steady state in a complete set of magnicon cavities, guaranteeing that physical and experimentally accessible solutions are obtained with power balance in each cavity. However, the steady-state code, in which power balance and the self-consistent RF phase are determined

2

either by iteration with varying electric fields and RF phases, or by feeding in values determined from the self-consistent time-dependent solutions, allows the detailed interactions in the cavities to be studied, and the beam phase space to be investigated in a systematic way. All of the particle codes make use of the phase synchronism that exists in the magnicon, in which the RF mode in each of the cavities rotates synchronously (except for a constant phase difference) with the RF mode of all the other cavities. (In the time-dependent code, this intercavity phase difference is permitted to evolve in time). This phase synchronism means that in steady state, the electrons entering the system at different times describe trajectories that are identical except for their spatial phase, and that the phase of the trajectories and the phase of the RF in all of the cavities advance together at the RF frequency of the deflection cavities. Thus, in steady state, the entire simulation may be carried out by following a single temporal slice of electrons that is one macroparticle deep in z. The time-dependent simulations make the same assumption, but allow the RF amplitude and phase in each cavity to evolve due to the interaction with the beam.

The use of steady-state simulations is discussed in detail in Ref. [4]. The use of steady-state simulations in combination with time-dependent simulations is discussed in Ref. [8]. The agreement between simulation and the INP magnicon experiment is discussed in Ref. [7].

The magnicon circuit consists of a drive cavity, a series of gain cavities, a penultimate cavity, and an output cavity. In the following

sections, we discuss the design of each of the cavities, and then discuss the design of the overall circuit.

III.   THE DRIVE AND GAIN CAVITIES

The new magnicon circuit employs drive and gain cavities identical to those in the previous NRL design. Figure 1(a) shows the RF electric field lines for the TM_{110} operating mode of the deflection cavities. [Note that the radial dimension is stretched by ~2.1× in this figure.] Figure 1(b) shows the transverse magnetic field on the axis of the first deflection cavity as a function of position along the axis, with a scale drawing of the cavity outline shown below it. The new circuit employs three gain cavities, one more than in the previous design, in order to increase the overall RF gain.

IV. PENULTIMATE CAVITY

The final deflection cavity, which is referred to as the penultimate cavity, is designed to carry out the final stage of beam spin up, in order to produce a high α beam for injection into the output cavity, where α is the ratio of transverse to parallel velocity with respect to the axial magnetic field. The penultimate cavity provides most of the beam transverse momentum. If the penultimate cavity followed the design of the gain cavities, it would contain RF fields that are substantially higher than the previous cavity, creating the likelihood of RF breakdown and substantial power dissipation due to Ohmic losses. The alternative to this is to find some means to spread the final stage of beam spin-up over more than one half of an RF wavelength. The approach taken in the previous NRL design [4], as

4

well as in the 7 GHz design of the INP [3], is to use an iris-coupled two-section penultimate cavity. Since this provides twice the interaction length, the spin up should require approximately half the RF field amplitude. The penultimate cavity used in the previous NRL design has two regions of high surface electric field: (1) the coupling iris, and (2) the aperture of the downstream or output beam tunnel. The maximum RF field on the beam tunnel can be mitigated by rounding of the aperture. However, the rounding of the iris is limited because increasing the iris thickness would decrease the coupling between the two sections. (The two sections must be strongly coupled in order to produce balanced RF fields in the presence of unequal beam loading.) In order to overcome these problems, we chose to investigate an alternative approach to the design of the penultimate cavity of the magnicon circuit, involving separate *uncoupled* cavities, as well as to investigate the optimization of the two-section *coupled* penultimate cavity.

A. Uncoupled penultimate cavities

The uncoupled penultimate cavities approach to the spin up of the electron beam would replace the two-section π-mode penultimate cavity of both the INP and NRL designs with a set of two or three *uncoupled* cavities, each of which should have approximately equal levels of RF field. This would be done by using a special spacing of the cavities to obtain a progressive spin up of the beam over a set of cavities, while avoiding the exponential growth of the RF field that occurs between successive gain cavities. This configuration has been previously described in the Russian literature [1], and is called the regime of "summing of the angles." However, the analysis in Ref. [1]

5

does not consider the effects of realistic cavity geometries, including the effects of beam tunnels, nor the nonlinear regime, in which the electron pitch angle becomes large. The "summing of the angles" approach has not been previously evaluated using particle simulations. If successful, this approach would avoid the complexity, and greater instability of a two-section coupled-cavity penultimate cavity, and might even allow the use of three cavities, further reducing the required rf fields. (Experiments and analysis undertaken at the INP have shown that the use of three *coupled* cavities as a penultimate cavity leads inevitably to instability.)

The evaluation of the uncoupled penultimate cavities began with the study of a single on-axis electron interacting with the fields of a cavity with small beam tunnels. For these initial simulations, the cavity fields corresponding to an ordinary gain cavity were employed (see Fig. 1), rather than the fields corresponding to the much larger beam tunnels required for transit of the spun-up electron beam. This is an ideal situation that should closely correspond to the linear analysis. Figure 2(a,b) shows simulation results for two uncoupled penultimate cavities, driven by a single gain cavity, and operating in the linear regime. Figure 2(a) shows the cavity outline, the trajectory of the single initially on-axis electron, and the spatial evolution of the electron pitch angle and the electron energy. The RF circuit is depicted as an overlapping sequence of discrete RF structures, such as are modeled in Fig. 1(b). Notice that the electron pitch angle increases in two steps, with approximately half of the total increase occurring in each of the penultimate cavities. However, the maximum pitch angle is only ~6°. Because the RF fields are weak, the electron

6

energy remains approximately flat. Figure 2(b) shows results from a time-dependent simulation of this configuration, with the amplitude versus time of the transverse magnetic field in each of the cavities. The field in the gain cavity was turned on with a risetime of 50 nsec. Notice that the asymptotic fields in the penultimate cavities are approximately equal. The simulations shown in Fig. 2(a,b) demonstrate that it is possible to achieve the theoretical predicted "summing of the angles" behavior for two ideal cavities for modest amounts of electron beam spin up. Figure 2(c,d) shows a set of similar simulations employing a single gain cavity followed by three penultimate cavities, operating in the linear regime. Again, the electron pitch angle increases in steps, with approximately one third of the increase occurring in each of the three penultimate cavities, and the time-dependent simulation shows that the fields in these three cavities are approximately equal. For both two and three cavities, with the intercavity spacing optimized according the formulas in [1] and [3], it was possible to equalize the fields in the separate cavities while the beam pitch ratio increased progressively through the cavities.

Figure 3 shows the result of attempting to operate in the same "summing of the angles" regime using a gain cavity and two penultimate cavities connected by beam tunnels large enough to permit passage of the spun-up electron beam. The cavity spacing in these simulations was optimized to equalize the RF fields in the two penultimate cavities. Figure 3(a) shows a steady-state simulation of the beam spin-up process with a transverse RF magnetic field H_r of 3000 A/m in the gain cavity. The pitch angle increases to ~8° in the

first penultimate cavity, and then drops to ~3° in the second penultimate cavity. Figure 3(b) shows the corresponding time-dependent simulation. Notice that the asymptotic amplitude of H_r in each of the penultimate cavities is ~20,000 A/m. Figure 3(c,d) shows similar simulations, but with a field of H_r=6000 A/m in the gain cavity, resulting in a field of H_r~40,000 A/m in the penultimate cavities. Again, the final pitch angle is lower than the pitch angle achieved after the first of the two penultimate cavities. (Note that the electron energy increase shown in the interior of the second penultimate cavity in Fig. 3(c) vanishes in the fringe fields of the cavity, and as the self-consistent, time-dependent simulations demonstrate, both penultimate cavities are in power balance.)

B. Coupled Penultimate Cavities

The objective of redesigning the penultimate cavity was to optimize the overall magnicon efficiency, as measured in the output cavity, while at the same time minimizing the RF electric field on the walls of the penultimate cavity. Optimizing the efficiency generally involves producing the desired degree of spin up of the electron beam ($\tan^{-1} \alpha$~55°) while at the same time minimizing the resulting energy spreads that degrade the output efficiency. Compared to the NRL magnicon circuit design described previously [4], four main changes were made in the design of the new penultimate cavity:

1. The output beam pipe diameter was reduced from 2.2 cm to 2 cm. This change takes advantage of the smaller maximum diameter of the spun-up electron beam for the planned experiment, due to the smaller initial beam diameter from the electron gun.

8

2. The length of the first section of the coupled cavity was reduced, in order to minimize a decrease in the beam α that occurs in the transition between the two sections of the cavity.

3. The rounding of the 4-mm-thick iris was changed from circular to elliptical to decrease the electric field enhancement. A radius of curvature increase here is not feasible because this would make the iris thicker, decreasing the coupling between the two sections of the cavity.

4. The rounding of the entrance to the beam tunnel was substantially increased, from a 2-mm radius of curvature to an 8-mm radius of curvature. This is the region of highest surface electric fields. However, increasing the rounding increases the effective length of the second section of the penultimate cavity, affecting the particle dynamics. For this reason, the rounding could only be optimized in conjunction with the particle simulation. The analysis of each cavity design involves an optimization versus axial magnetic field that maximizes the transverse velocity $v_\perp$ and minimizes the rf magnetic field H_r.

Figure 4 shows a plot of the calculated maximum surface electric field enhancement in the penultimate cavity as a function of the rounding radius of the output aperture. The field enhancement factor is calculated relative to the maximum surface field in an ideal cavity with no apertures having the same maximum on-axis value of the transverse magnetic field. This enhancement factor decreases monotonically as the rounding radius is increased from 2 mm (the old value) to 10 mm. However, based on particle simulations employing realistic electron beam radii, the 8-mm rounding radius was selected

9

for the final circuit, because the 10-mm rounding radius case was less effective in spinning the beam up.

Figure 5 shows RF fields in the old version of the TM_{110} π-mode penultimate cavity. Figure 5(a) shows a plot of transverse RF magnetic field on axis versus axial position, and also shows a scale drawing of the cavity cross section. Figure 5(b) shows the surface RF fields (normal electric field and tangential magnetic field) calculated along the inner surface of the cavity for a stored energy of 1 mJ in the standing wave. Notice that the highest surface electric field amplitude of ~4.1 MV/m occurs towards the right side of this figure, at a position corresponding to the 2-mm radius-of-curvature entrance to the 2.2-cm-diam. output beam tunnel. Notice also the large field enhancement "rabbit ears" in the middle of the figure at positions corresponding to the two sides of the rounded aperture through the iris. (These sharp features persist in very high mesh density studies of the surface RF fields.) However, the maximum surface field in this region is not as high as at the output aperture. Figure 5(c) shows the cavity RF electric field lines for the TM_{110} π-mode.

Figure 6 shows the RF fields for the version of the new penultimate cavity design that uses a standard 2-mm radius of curvature penultimate cavity iris aperture. This iris design is identical to that used in the old version of the penultimate cavity. Figure 6(a) shows a plot of transverse RF magnetic field on axis versus axial position, and also a scale drawing of the cross section of the new penultimate cavity. The additional rounding of the entrance to the output beam tunnel is readily apparent. Figure 6(b) shows the RF fields calculated along the inner surface of this cavity for a stored

energy of 1 mJ in the standing wave. The peak surface electric field has been reduced to ~3.6 MV/m. Once again, there are large field enhancement "rabbit ears" in the middle of the figure at positions corresponding to the two sides of the rounded iris aperture. In this case, the "rabbit ears" are more symmetric, and once again the fields in this region are not as high as at the output aperture. Figure 6(c) shows the cavity RF electric field lines for the TM_{110} π-mode.

Figure 7 shows the RF fields for the alternative version of the new penultimate cavity design that uses an elliptically rounded penultimate cavity iris. The ellipse has a 2:1 aspect ratio. The RF field profile in Fig. 7(a) is virtually identical to that of Fig. 6(a). Figure 7(b) shows the RF fields calculated along the inner surface of this cavity for a stored energy of 1 mJ in the standing wave. The maximum surface electric field is again ~3.6 MV/m, since the rounding of the entrance to the output beam tunnel is identical to that shown in Fig. 6. However, the "rabbit ears" in the middle of the figure have been substantially reduced. As a result, the maximum electric field on the elliptical iris is now 11% lower than on the rounded iris. Figure 7(c) shows the cavity RF electric field lines for the TM_{110} π-mode of this cavity. This is almost identical to the field pattern of Fig. 6. The very close correspondence between Fig. 6(a,c) and Fig. 7(a,c) is important, because the particle simulations discussed later in this section were carried out for the first version of the new penultimate cavity. The alternative elliptically rounded version can be expected to work almost identically, but with 11% lower surface fields in one critical region of the magnicon circuit. An additional advantage of the elliptically rounded iris is a 12% increase in the coupling coefficient [4] between

11

the two sections of the cavity (0.73% instead of 0.65%), because the effective wall thickness is decreased.

While the effects of all these changes to the penultimate cavity design are coupled together, our conclusion is essentially that change 2 increases the "efficiency" of the spin-up in the penultimate cavity, allowing a decrease in the on-axis transverse RF magnetic field, while changes 1, 3, and 4 reduce the surface electric field enhancement for a given value of transverse magnetic field on axis. The overall result is a reduction from a maximum surface electric field of 670 kV/cm in the original NRL design to a new value of 572 kV/cm. This new value is comparable to values employed in high power X-band klystrons at SLAC, and should be acceptable. The maximum electric field on the rounded iris aperture is 532 kV/cm, and this is reduced to 472 kV/cm for the elliptically-rounded aperture.

V. OUTPUT CAVITY

In order to improve the efficiency and lower the maximum surface electric fields, the output cavity was also redesigned. This entailed: 1) reducing the beam tunnel diameter from 2.2 cm to 2 cm, 2) increasing the rounding of the beam tunnel apertures at both ends of the cavity from 2-mm radius of curvature to 8-mm radius of curvature, and 3) changing the total length of the cavity from 5 cm to 4 cm. In this case, change 3 reduced the RF field required to decelerate the electron beam by changing the axial distribution of RF fields, while changes 1 and 2 reduced the maximum surface RF field enhancement for that value of transverse magnetic field.

Figures 8 and 9 show the RF fields for the old and new versions of the output cavity. Figure 8(a,b) shows the transverse RF magnetic field and the axial RF electric field calculated at a radius of 0.5 cm along the length of the old output cavity, while Fig. 8(c) shows the RF electric field lines for the TM_{210} operating mode of this cavity. Figure 9 shows the same plots for the new cavity. Notice that the shorter length of the new output cavity, combined with the effects of the additional rounding, has had a significant effect on the axial structure of the operating mode: the RF fields of Fig. 9(a) are significantly more peaked in the center of the cavity than those of Fig. 8(a). An investigation of these two geometries via particle simulations has shown that the center-peaked transverse magnetic field profile shown in Fig. 9(a) requires lower RF fields in the cavity, reducing both the ohmic losses and the maximum electric field at the wall, and also results in higher efficiency.

The magnicon simulation codes cannot directly handle cavity boundaries that are not cylindrically symmetric. Thus, they cannot directly model the effect of the two waveguides that couple power out from the output cavity, and the possible effect of this lack of quadrupole symmetry on the operating TM_{210} mode. This important subject is discussed in the next section.

A. Study of Side-Coupling from the Output Cavity

The NRL frequency-doubling magnicon amplifier employs a quadrupole (TM_{210}) mode in the output cavity at 11.424 GHz, which in the simplest pillbox approximation corresponds to a radius of ~2.1 cm. In this approximation, the fields are uniform along the entire

13

length of the cavity. When the effects of beam tunnels are included, as seen in Figs. 8 and 9, the ideal TM_{210} fields are substantially modified. The electromagnetic codes employed in the steady-state and time-dependent simulations of magnicon operation are limited to cylindrically symmetric structures, but can handle the full three-dimensional fields of the non-symmetric magnicon modes. Such simulations are appropriate to the present experiments at NRL, in which end coupling is employed as the means for extracting RF from the output cavity.

However, since the earliest days, the INP experiments have employed side coupling to extract RF power. The advantage of this approach is that the radiation is immediately separated from the electron beam collector, and emerges in fundamental-mode X-band waveguide. Unfortunately, the asymmetry introduced by the side-coupling ports can induce azimuthal variations in the field that may adversely affect the beam dynamics.

For purposes of calculating the output coupling, the rotating quadrupole mode of the output cavity must be modeled as two non-rotating modes separated by 45° of rotation about the cavity axis and by a phase difference of $\pi/2$. The INP magnicon design employs two standard rectangular waveguides that are separated by 135° in order to couple to both of the non-rotating components composing the rotating TM_{210} mode. The INP group has made use of a two-dimensional electromagnetic field solver, treating the output cavity as infinitely long, to design the output cavity in such a way as to minimize mode conversion into dipole modes caused by the output waveguides. Such mode conversion may be highly deleterious, since 1) dipole modes are

14

not cut off in the beam tunnels, and can leak into the penultimate cavity, interfering with the beam spin up, and 2) a dipole component in the fields of the output cavity can lower the efficiency of electron deceleration. In all of the experiments to date, the INP output cavity has included two "protrusions," separated by 45° from each of the output waveguides, in order to help symmetrize the RF mode, and has also employed a number of tuning stubs with which to minimize the dipole component. However, recent experiments have demonstrated the inadequacy of this approach [7].

The most recent INP design [7] employs a total of six protrusions around the circumference of the cavity, so that, counting the two protrusions that lead into output waveguides, there are a total of eight protrusions, spaced every 45°. Two waveguides, separated either by 45° or 135°, is the minimum number of waveguides that can be used to couple power out of the rotating quadrupole mode, and eight protrusions is the minimum number of protrusions that can preserve the symmetry of the rotating quadrupole mode.

We have chosen to employ an output cavity design similar to that presented in [7], but scaled in size to operate at 11.424 GHz. We have carried out detailed two-dimensional simulations of this configuration using the code CFISH [9], taking the cavity length to be infinite. To mock up the outgoing-wave boundary condition, a dielectric was inserted at the end of the rectangular waveguides with properties that lead to complete evanescence of the RF that leaks into the waveguides from the cavity. In reality, the beam tunnels at the ends and the finite axial extent of the protrusions and of the rectangular waveguides will cause the actual cavity frequency and loading to be somewhat different

15

from that calculated by means of the two-dimensional simulations. Therefore, the initial design obtained with the aid of CFISH must be refined, either by means of three-dimensional codes or by experimental cold test.

Figure 10 (top) shows the cavity cross section and H' and H'' field lines obtained with CFISH. (Here, H' and H'' denote the real and the imaginary parts of the RF magnetic field H. The magnetic field is represented by a complex number because the dielectric in the waveguide induces a phase shift in the magnetic field.) Due to reflection symmetry, only one half of the cavity need be modeled. In an ideal, cylindrically-symmetric cavity, the two orthogonal non-rotating modes would be degenerate. The result of the output coupling waveguides is to break this degeneracy. The purpose of adding the six additional protrusions is, so far as possible, to restore the degeneracy. By choosing the boundary conditions on the midplane, one can force the code to find one or the other of the two modes. The boundary conditions in Fig. 10 (left) lead to magnetic field lines parallel to the symmetry plane. The frequency of this mode is 11.3856 GHz and the quality factor is 624. (For the desired cavity structure, the waveguides occupy only one quarter of the cavity length and therefore the Q would be about 4 times higher than the CFISH estimate.) Figure 10 (bottom left) shows the plot of $|H|$ and H_x as functions of the distance from the origin of the cavity along the arm that extends into the waveguide. (H_x denotes the electric field along the arm, and $|H|$ denotes the magnitude of the complex value of the magnetic field.) Notice that $|H|$ is constant in the X-band waveguide in the region between the iris and the lossy dielectric boundary. This

indicates a good match into the dielectric, and thus a good approximation to an outgoing-wave boundary condition. Figure 10 (top right) shows the cavity cross section for the second mode. Here, the boundary conditions force the magnetic field lines to be normal to the symmetry plane. The frequency of this mode is 11.3819 GHz and the quality factor is 627. Figure 10 (bottom right) shows the plot of $|H|$ and H_x along the arm.

Note that the frequencies and quality factors of the two modes are very close. This has been accomplished by appropriate choice of dimensions for the cavity protrusions and for the iris coupling the cavity to standard WR-90 X-band waveguide. We have thus obtained mode frequencies that are well within their $1/Q$ bandwidths. By choosing the proper dimensions, one can thus ensure that the two degenerate modes are sufficiently close so that both can be simultaneously excited to generate a rotating TM_{21} mode. Furthermore, simple scaling of the cavity dimensions will permit us to obtain the desired frequency of 11.424 GHz. Additionally, the field line plots in Fig. 10 clearly display the quadrupole nature of the modes found by CFISH, with no noticeable admixture of a dipole component.

VI.   DISCUSSION OF THE ELECTRON GUN AND FINAL MAGNICON
       CIRCUIT

Figure 11 shows the overall configuration of the new magnicon circuit, including cross sections of the magnicon cavities, the coils, and the iron magnet yoke. The new circuit consists of a drive cavity, three simple gain cavities, a redesigned two-section π-mode penultimate cavity, all operating in the TM_{110} mode at 5.712 GHz,

17

and a new output cavity operating in the TM_{210} mode at 11.424 GHz. As part of the redesign, the overall magnicon gain has been increased from the previous value of 48 dB to 57 dB by the addition of an extra gain cavity. The additional gain cavity reduces the required drive power for a 50 MW device to 80 W at 5.712 GHz. This gain is consistent with values employed in the design of X-band klystrons at SLAC for use in the NLC [10]. Figure 11 also shows the axial magnetic field along the axis of the magnicon. A set of realistic (manufacturable) current-carrying coils, as illustrated, was used to produce the desired axial magnetic field profile in the simulations. [Note that the coils carry equal currents, except for the fifth coil, which carries no current. Varying the current in the fifth coil can be used to shape the magnetic field profile in the vicinity of the output cavity, in order to optimize the efficiency.]

The point design for the 11.424 GHz magnicon amplifier involves use of a 500 kV, 200 A, 2-mm diameter electron beam. The electron gun to produce this beam will be a novel high convergence relativistic Pierce gun using a dispenser cathode. A preliminary design for this electron gun has been completed by R.B. True and G.R. Good of Litton Systems Inc. [see Fig. 12]. The gun will operate for pulse lengths of 1 μsec at low duty factor. (In fact, the gun has been designed with a maximum focus electrode gradient of less than 190 kV/cm, in order to permit operation at pulse lengths of 2 μsec or more, and it should be fully capable of high duty factor operation.) Beam compression in the gun must necessarily be high in order to limit the field gradient off the focus electrode and to limit cathode loading in order to produce a long operating lifetime for the tube. A

7.5-cm diameter, 30° half-angle cathode was used, implying an overall compression ratio of 1400:1 and a mean cathode loading of 4.5 A/cm^2. One unique feature of the gun is that it includes an electrically-isolated focus electrode element adjacent to the cathode, which is used to control the beam edge discharge angle, and to completely eliminate emission from the outer cathode cylinder, both of which can give rise to unwanted halo electrons outside of the main beam core. This electrode will be biased negatively by a few hundred volts with respect to the cathode potential. This design will be discussed in detail elsewhere [11]. Final design and construction of the gun is to commence forthwith.

However, the exact beam parameters will only be known when the electron gun is built and installed in its modulator, the beam carefully matched into the magnicon magnet, and the beam properties optimized and measured. Accordingly, design calculations have been carried out for three possible beam diameters, 1.5 mm, 2.0 mm, and 2.5 mm. The Brillouin diameter for a 200 A, 500 kV beam in a magnetic field of 6.5 kG is ~1.2 mm. Full design calculations were carried out for each beam diameter, with the circuit gain, the axial magnetic field, and output cavity Q-factor separately optimized for each case.

Figure 13 shows a set of steady-state and time-dependent simulations of the complete magnicon circuit for a 2.0-mm-diam. electron beam. Figure 13(a) and 13(b) show the results of steady-state simulations employing 37 macroparticles. (The convergence of these simulations has been verified using runs employing up to 177 macroparticles.) Figure 13(a) shows the spatial evolution of the

19

energy of these macroparticles, all of which begin at the left of the figure at 500 keV. Figure 13(a) also follows the electron trajectories through a scale drawing of the RF cavities. The transverse dimension has been stretched by 4× in order to show the details of the orbits. The beam scalloping that is evident is a result of simulating a zero canonical momentum beam in the absence of space charge, and represents an unmatched beam. Notice that energy spreads and large energy excursions take place in the region of the penultimate cavity, but that the energy loss in the output cavity is remarkably uniform. (Note that the apparent electron energy gain in the second section of the penultimate cavity does not violate the power balance requirement—there is a continuing interaction with the fringing fields of this cavity that results in a net energy loss from the beam that is in balance with the ohmic losses in the walls of the penultimate cavity.) The result is a predicted efficiency of 58.6%. Figure 13(b) shows the spatial evolution of the electron pitch angle. There is an initial spread in pitch angle, due to the assumption of zero canonical angular momentum, but the spin up process has a high degree of coherence. Nevertheless, there is a large spread in pitch angle by the end of the output cavity.

Figure 13(c) shows a self-consistent time-dependent simulation of the entire magnicon circuit. The traces originating at 0 are, from top to bottom at the right hand side of the figure: the output cavity RF magnetic field amplitude, the penultimate cavity RF magnetic field amplitude, and the RF magnetic field amplitudes for the third, second, and first gain cavities. The RF field for the drive cavity is indistinguishable from the baseline. The axial values of the RF fields

for the deflection cavities are specified in units of Am^{-1}. However, since the RF magnetic field is zero on axis for the quadrupole operating mode of the output cavity, the RF field strength for the output cavity is specified by the on-axis value of the derivative of the transverse RF magnetic field. This has been expressed in $Am^{-1}cm^{-1}$ in order to permit plotting on the same vertical scale as the deflection cavity fields. The trace originating at the upper left of the figure is the RF phase of the output cavity. Notice that it changes rapidly during the "turn-on" of the magnicon circuit, put reaches a steady-state value after 0.6 μsec that indicates a stable and converged solution. The RF amplitudes and phases from the time-dependent solution were used in the steady-state simulation of Fig. 13(a,b). The cavity Q-factor assumed in this simulation was 300.

Figure 14(a,b) shows a set of steady-state and time-dependent simulations of the final magnicon circuit for a 1.5-mm-diam. beam. The result is very similar to the simulation results of Fig. 13. However, the optimized RF field in the output cavity is slightly lower (on-axis transverse H-field gradient $\sim 1.33 \times 10^5$ $Am^{-1}cm^{-1}$ versus ~ 1.55 $Am^{-1}cm^{-1}$), and the ultimate efficiency is slightly higher (60.4%). Figure 14(c,d) shows a comparable set of simulations for a 2.5-mm-diam. beam. In this case, the electron trajectories in the output cavity are noticeably less coherent, and there is a larger spread in the final electron energy distribution. As a result, the efficiency falls to ~53%.

Figure 15 summarizes the results of the simulations shown in Figs. 13 and 14. Clearly, the ultimate magnicon efficiency depends critically on the initial beam radius. This strong dependence of

efficiency on beam radius requires the use of an electron beam with a radius as close as possible to the Brillouin radius.

The result of the redesign process has been to apply more accurate simulation models to the optimization of the magnicon circuit for use with a near-Brillouin-radius thermionic electron beam. The previous NRL 11.4 GHz magnicon circuit was optimized for a much larger electron beam. (Furthermore, the simulations were carried out using simulation models that tended to underestimate the surface RF field enhancements.) For the "same" 2-mm-diam. electron beam, the predicted efficiency has increased from 55.6% to 58.6%, while at the same time the maximum surface RF field in the penultimate cavity has been reduced from 670 kV/cm to 570 kV/cm, and the maximum surface RF field in the output cavity has been reduced from 830 kV/cm to 520 kV/cm.

In order to examine the stability of the output cavity interaction against variation of parameters, a study was made of efficiency versus RF field in the output cavity. In a self-consistent model, this is equivalent to a variation in the output cavity quality factor, since power balance will determine the RF field in the output cavity. As seen in Fig. 16, the efficiency varies by less than 0.5% as the RF field is varied over the interval 1.45–1.55×10^7 Am^{-2}.

Figure 17 shows a conceptual schematic of the entire magnicon amplifier, including the electron gun, the magnet, the iron yoke, the magnicon cavities, and the collector. Figure 17 also presents a table of values for the final magnicon design.

VII. SUMMARY

We have designed a circuit for a high gain, high efficiency 11.424 GHz frequency-doubling magnicon amplifier driven by a 500 kV, 200 A, 2-mm-diameter thermionic electron beam. The predicted efficiency is greater than 58%, at a maximum surface RF electric field of 570 kV/cm, a value that we believe is consistent with design values in other high power X-band amplifier tubes. This design forms the basis of a new thermionic magnicon experiment, which we plan to assemble and test at NRL in the near future.

As a part of the redesign process we evaluated the use of uncoupled penultimate cavities, in place of the coupled two-section penultimate cavity used in the previous NRL and INP designs. It was found to be generally true that when the cavity spacing was adjusted to produce equal RF fields in a set of two or three cavities, the resulting self-consistent RF phases in the cavities did not lead to progressive spin up of the electron beam. For that reason, an improved version of the two-section penultimate cavity was retained in the present design.

REFERENCES

1. M. Karliner, E.V. Kozyrev, I.G. Makarov, O.A. Nezhevenko, G.N. Ostreiko, B.Z. Persov, and G.V. Serdobintsev, "The Magnicon— An Advanced Version of the Gyrocon," *Nucl. Instrum. Methods Phys. Res.*, vol. A269, pp. 459-473, 1988.

2. W.M. Manheimer, "Theory and Conceptual Design of a High-Power Highly Efficient Magnicon at 10 and 20 GHz," *IEEE Trans. Plasma Sci.*, vol. 18, pp. 632-645, 1990.

3. O.A. Nezhevenko, "Gyrocons and Magnicons: Microwave Generators with Circular Deflection of the Electron Beam," *IEEE Trans. Plasma Sci.*, vol. 22, pp. 765–772, October 1994.

4. O.A. Nezhevenko, V.P. Yakovlev, S.H. Gold, and B. Hafizi, "Design of a High Power, X–Band Magnicon Amplifier," *IEEE Trans. Plasma Sci.*, vol. 22, pp. 785–795, October 1994.

5. N.C. Jaitly, M. Coleman, S. Eckhouse, A. Ramrus, S.H. Gold, R.B. McCowan, and C.A. Sullivan, "1 MV Long Pulse Generator with Low Ripple and Low Droop," in *Digest of Technical Papers—Eighth IEEE International Pulsed Power Conf.*, IEEE Catalog No. 91CH3052–8, edited by K. Prestwich and R. White (IEEE, New York, 1991), pp. 161–165.

6. S.H. Gold, A.K. Kinkead, A.W. Fliflet, B. Hafizi, and W.M. Manheimer, "Initial Operation of a High Power, Frequency-Doubling X–Band Magnicon Amplifier," *IEEE Trans. Plasma Sci.*, June, 1996, in press.

7. E.V. Kozyrev, I.G. Makarov, O.A. Nezhevenko, B.Z. Persov, G.V. Serdobintsev, S.V. Shchelkunoff, V.V. Tarnetsky, V.P. Yakovlev,

and I.A. Zapryagaev, "Performance of the High Power 7 GHz Magnicon Amplifier," *Part. Accel.*, in press.

8. V. Yakovlev, O. Danilov, O. Nezhevenko, and V. Tarnetsky, "Numerical Simulation of Magnicon Amplifier," in *Proc. 1995 Particle Accelerator Conf.*, in press.

9. "Reference Manual for the POISSON/SUPERFISH Group of Codes," Los Alamos Publication LA-UR-87-126 (1987).

10. E. Wright, R. Callin, G. Caryotakis, K. Eppley, K. Fant, R. Fowkes, S. Gold, R. Koontz, R. Miller, C. Pearson, R. Phillips, S. Tantawi, and A. Vlieks, "Design of a 50 MW Klystron at X-band," in *Pulsed RF Sources for Linear Colliders—AIP Conference Proceeding 337*, edited by R.C. Fernow, AIP Press, New York, 1995, pp. 58-66.

11. R.B. True and G.R. Good, "Design of a Very High Convergence 500 kilovolt Gun for the NRL X-Band Magnicon," to be presented at the 1996 Microwave Power Tube Conference, Monterey, CA, May 1996.
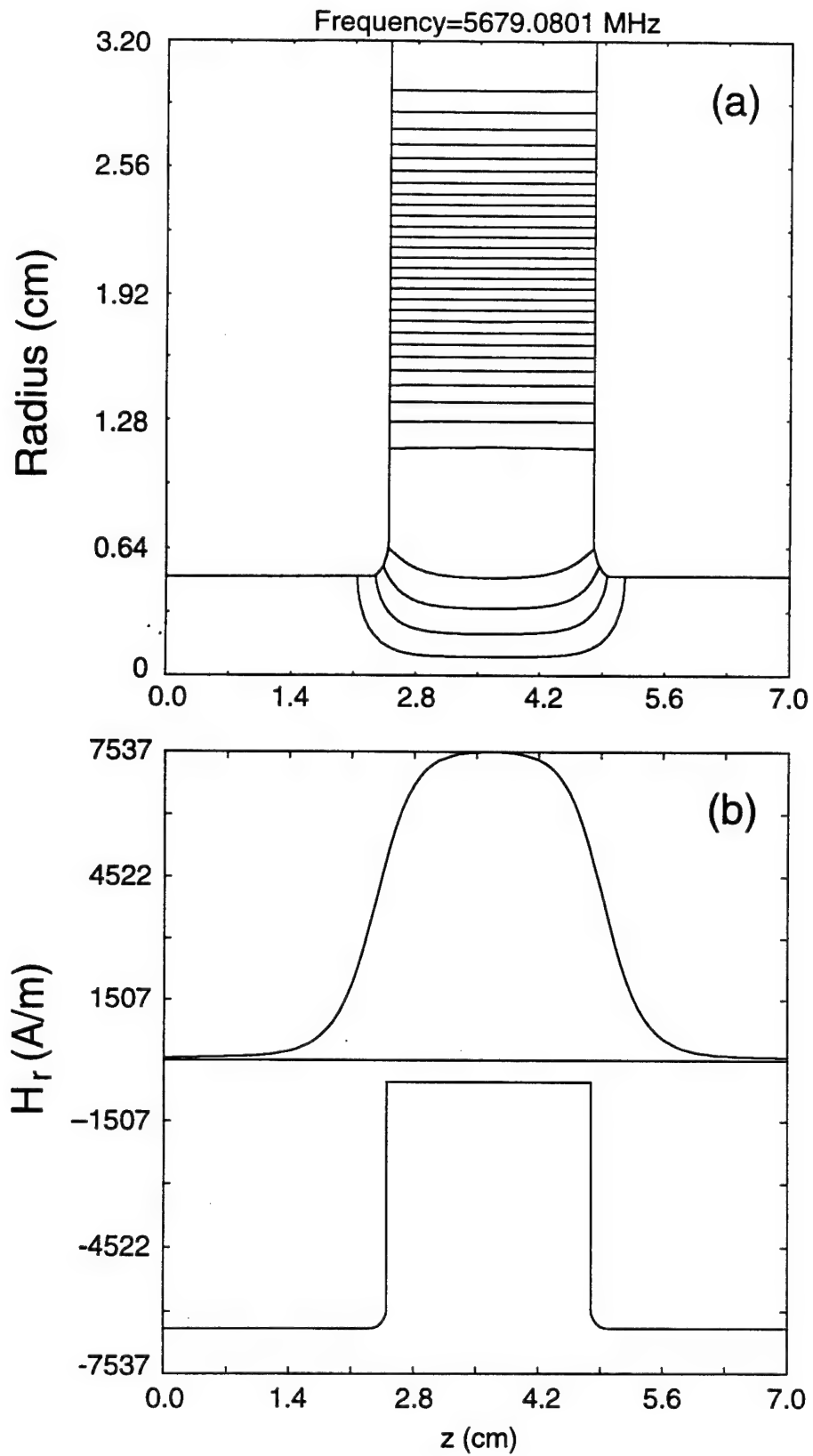
Fig. 1. (a) RF electric field lines in the half-wavelength TM_{110} deflection cavities; (b) transverse magnetic field on the axis of the first deflection cavity as a function of position along the axis.
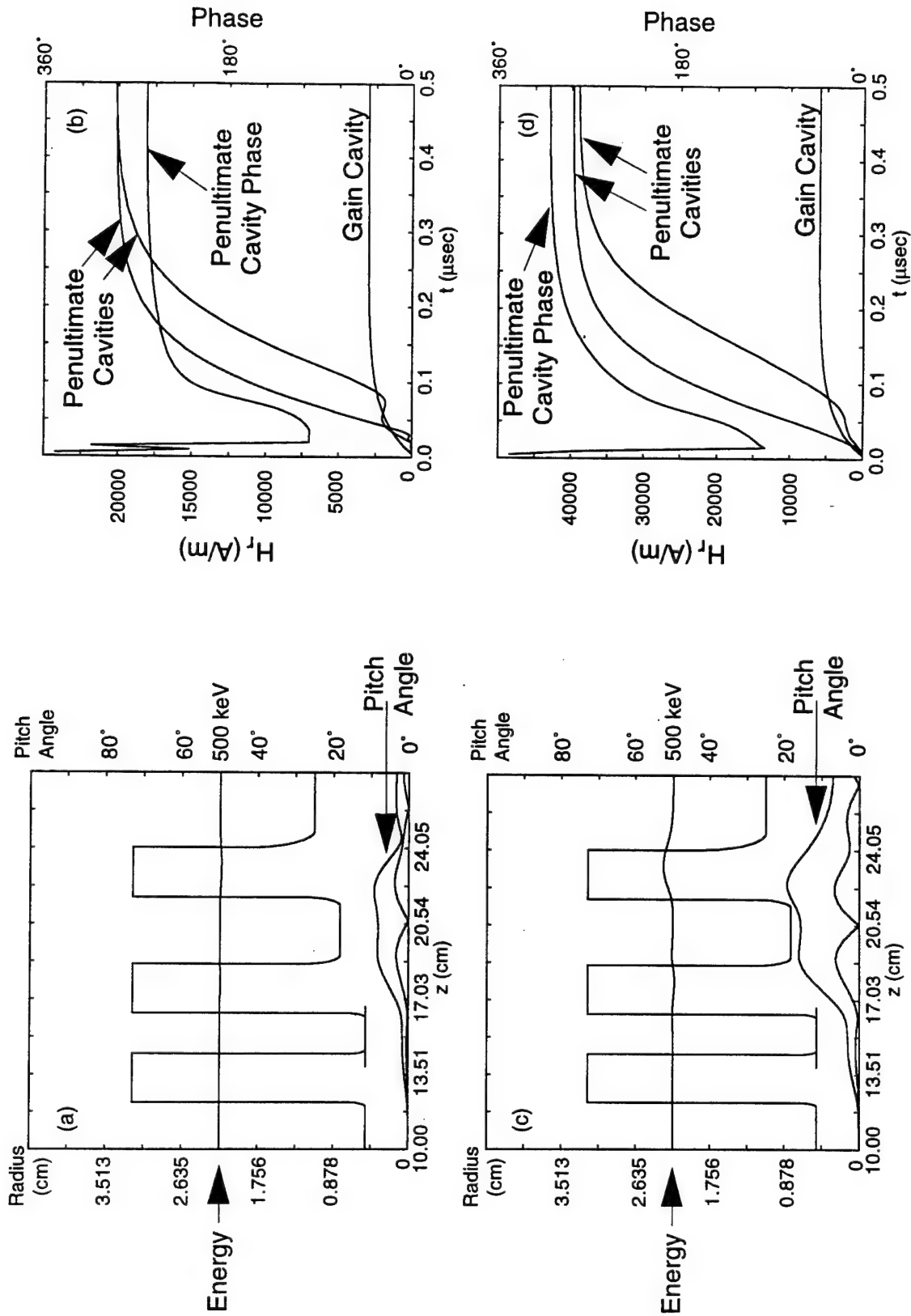
Fig. 2. Single-particle simulations of one gain cavity and two or three uncoupled penultimate cavities with small beam tunnels operating in the "summing of the angles" regime: (a) Steady-state simulation for one gain cavity and two penultimate cavities, showing electron trajectory, pitch angle, and energy versus z. The cavity outlines are also shown, with the radial dimension expanded by 4×. (b) The corresponding time-dependent simulation, showing transverse magnetic field amplitude versus time for each cavity and the rf phase in the last cavity. (c,d) Steady-state and time-dependent simulations for one gain cavity and three uncoupled penultimate cavities.

Fig. 3. Single-particle simulations of one gain cavity and two uncoupled penultimate cavities with "realistic" beam tunnels operating in the "summing of the angles" regime:
(a,b) Steady-state and time dependent simulations for H_r=3000 A/m in the gain cavity;
(c,d) Steady-state and time dependent simulations for H_r=6000 A/m in the gain cavity.

28
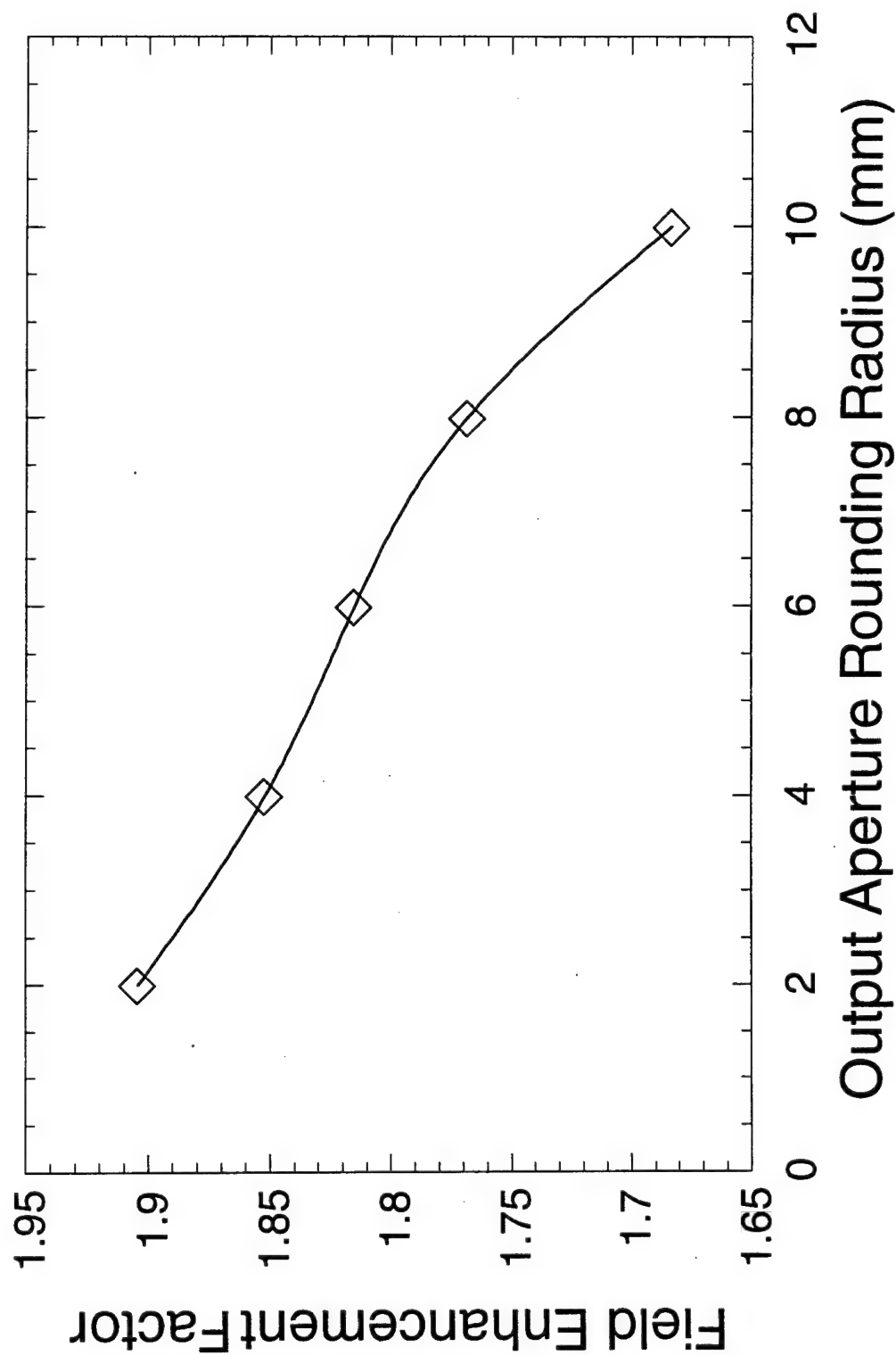
Fig. 4. Calculated penultimate cavity maximum surface electric field enhancement factor versus rounding radius of the output aperture. The field enhancement is calculated relative to an ideal cavity with no apertures having the same maximum on-axis value for the transverse magnetic field.

Frequency=5601.0005 MHz

(a)

H_r (kA/m)

(b)

H_t (kA/m)

E: —
H: —

E (MV/m)

(c)

Radius (cm)

z (cm)

L (cm)

z (cm)
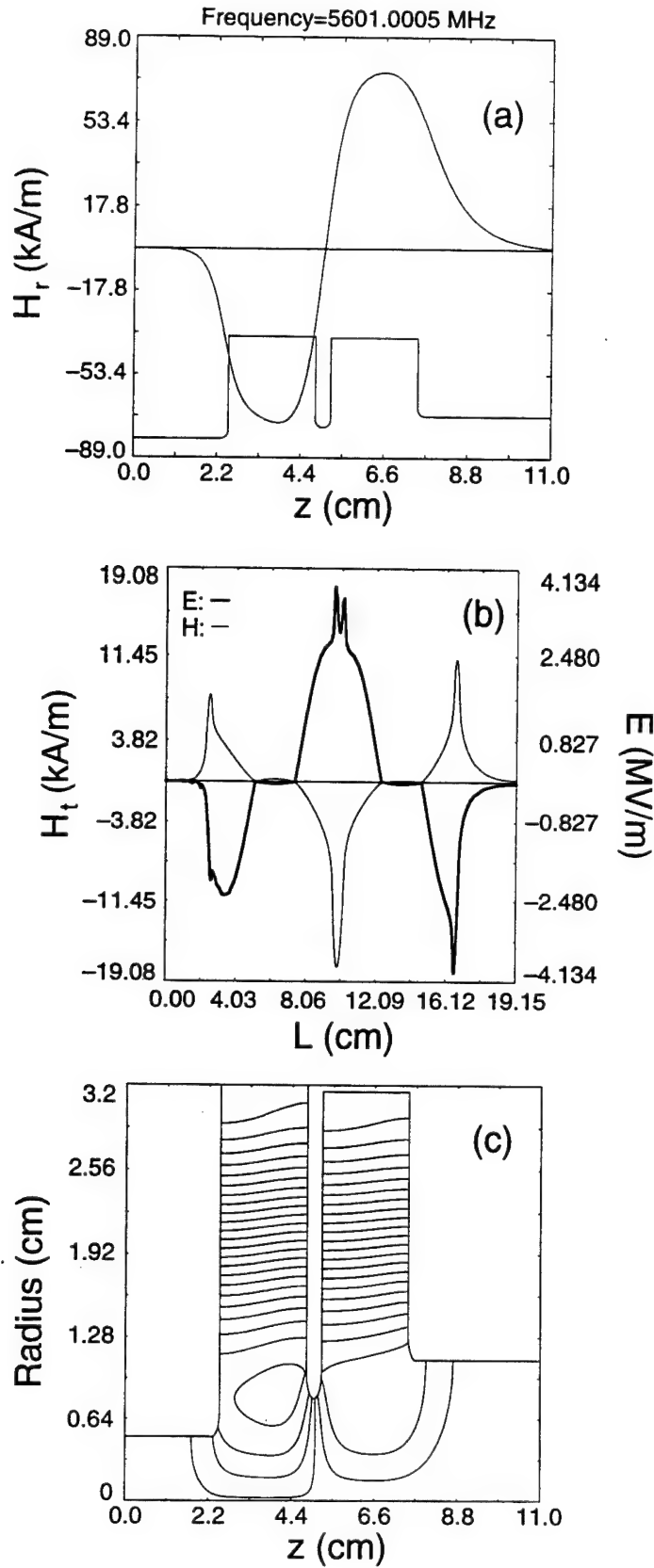
Fig. 5. RF fields in the old TM $_{110}$ π-mode penultimate cavity: (a) Transverse magnetic field on axis as a function of position along the axis; (b) Normal electric and transverse magnetic fields along the inner surface of the cavity; (c) RF electric field lines .

30
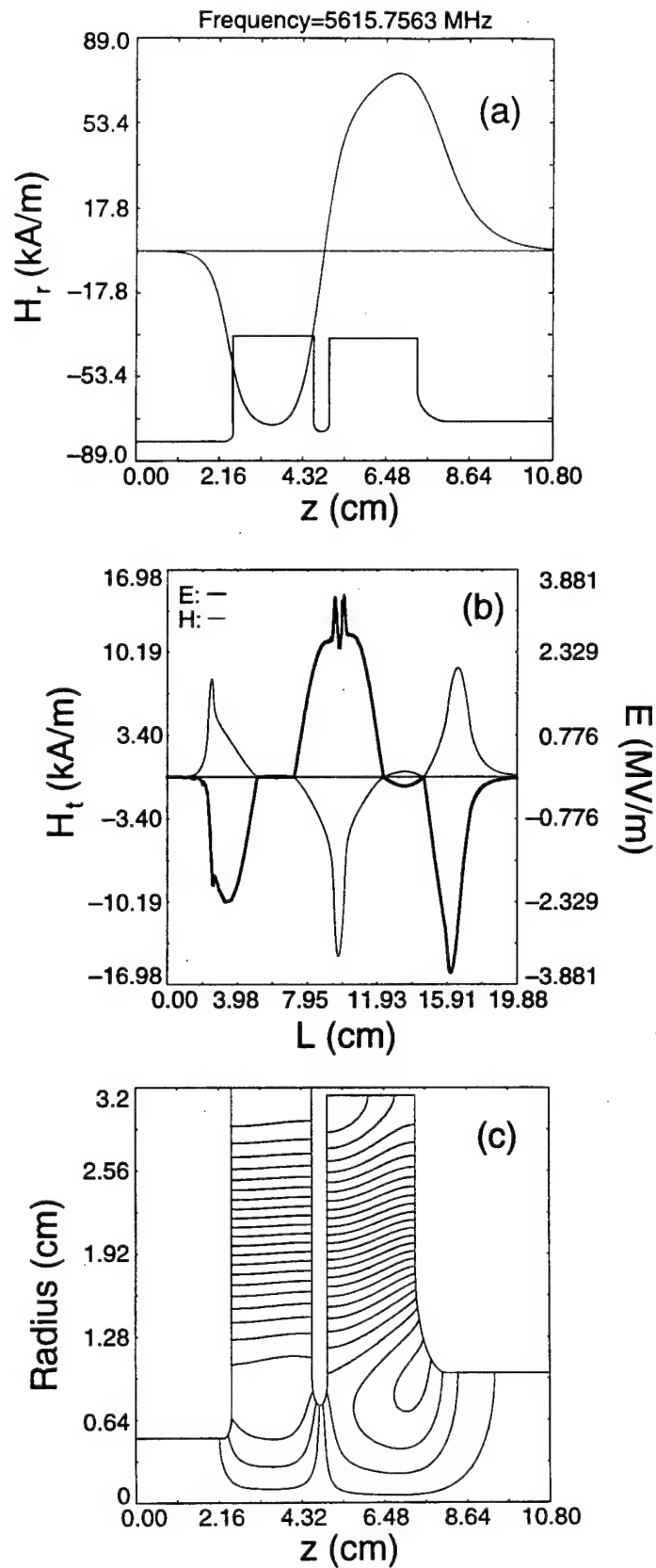
Fig. 6. RF fields in the new TM_{110} π-mode penultimate cavity with a
2-mm-radius of curvature rounded penultimate cavity iris: (a) Transverse
magnetic field on axis as a function of position along the axis; (b) Normal
electric and transverse magnetic fields along the inner surface of the cavity;
(c) RF electric field lines .

Frequency=5602.7227 MHz

89.0

53.4

17.8

−17.8

−53.4

−89.0

(a)

0.00   2.16   4.32   6.48   8.64   10.80

z (cm)

18.79   E: —   3.758
           H: —   (b)

11.27   2.255

3.76   0.752

−3.76   −0.752

−11.27   −2.255

−18.79   −3.758

0.00   3.97   7.93   11.90   15.87   19.83

L (cm)

3.2

2.56   (c)

1.92

1.28

0.64

0

0.00   2.16   4.32   6.48   8.64   10.80

z (cm)
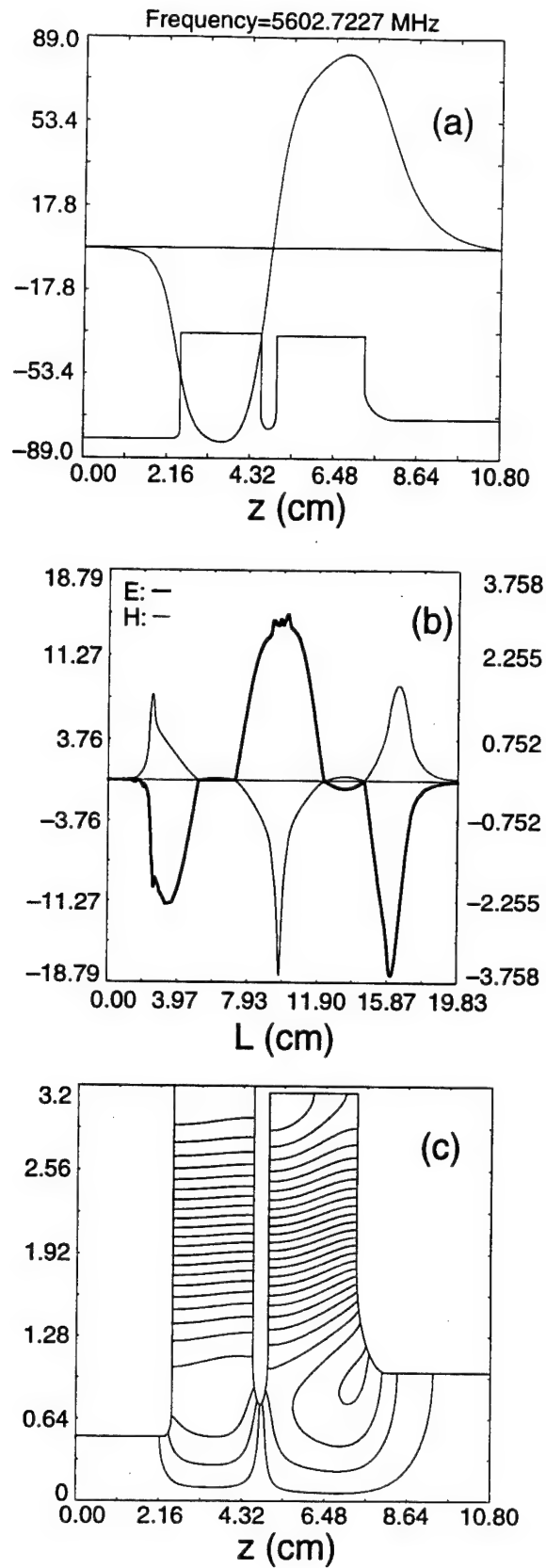
Fig. 7. RF fields in the new TM $_{110}$ π-mode penultimate cavity for an elliptically rounded penultimate cavity iris with a 2:1 aspect ratio: (a) Transverse magnetic field on axis as a function of position along the axis; (b) Normal electric and transverse magnetic fields along the inner surface of the cavity; (c) RF electric field lines .
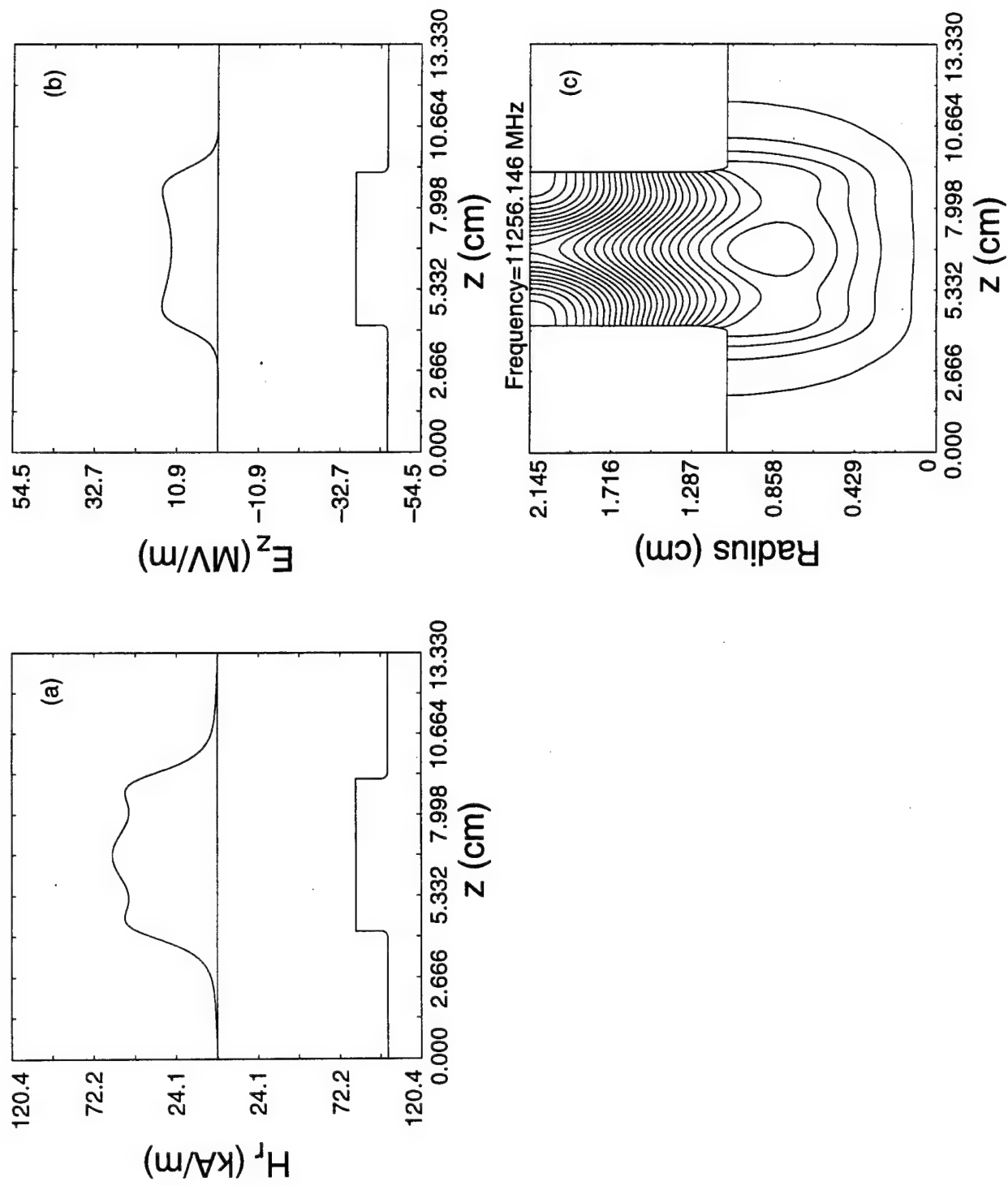
Fig. 8. RF fields in the old TM_{210} output cavity: (a,b) Transverse magnetic and longitudinal electric fields at a radius of 0.5 cm versus axial position; (c) RF electric field lines.
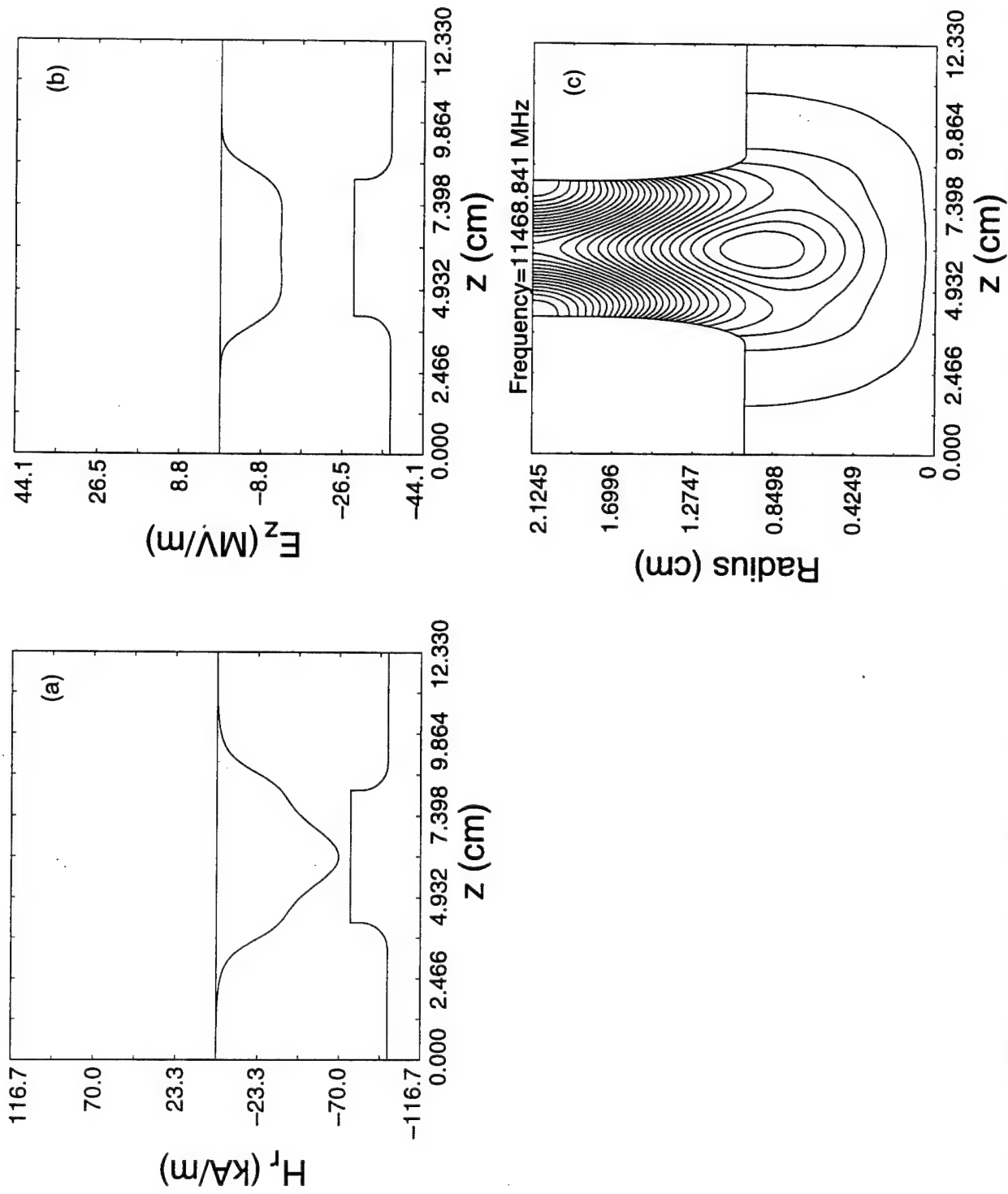
Fig. 9. RF fields in the new TM$_{210}$ output cavity: (a,b) Transverse magnetic and longitudinal electric fields at a radius of 0.5 cm versus axial position; (c) RF electric field lines.

34

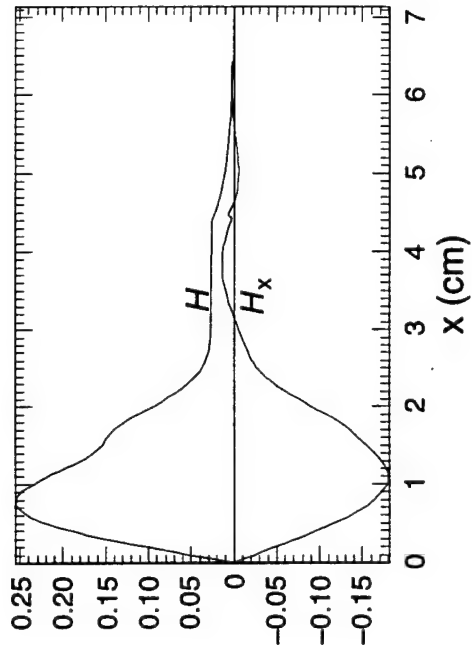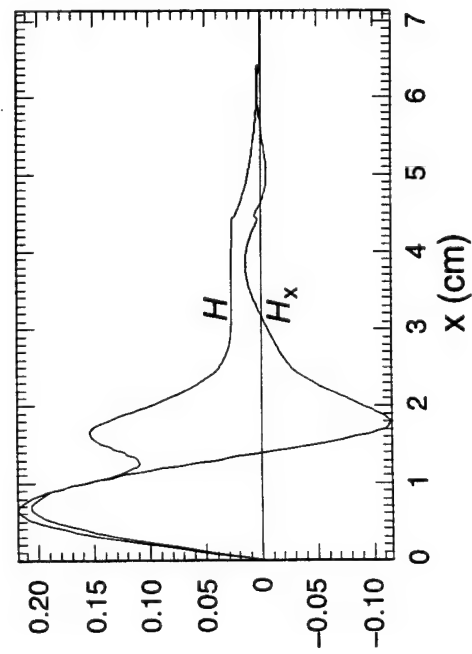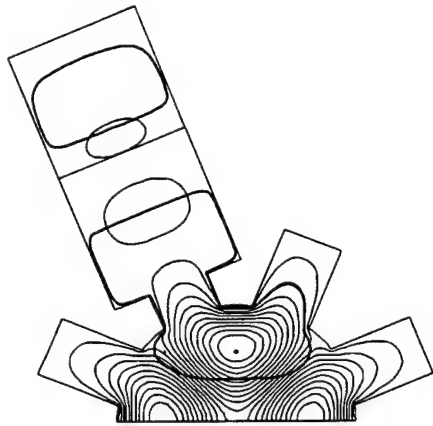Frequency=11385.574 MHz
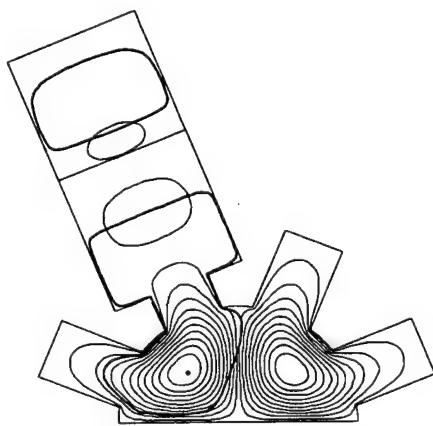
Frequency=11381.946 MHz

Fig. 10. CFISH simulation of the TM_{210} modes of the output cavity with magnetic field lines (left) parallel to the symmetry plane, and (right) normal to the symmetry plane: (top) RF magnetic field (H) lines, (bottom) plot of $|H|$ and H_x measured outward along the radius leading from the origin through the X-band waveguide.
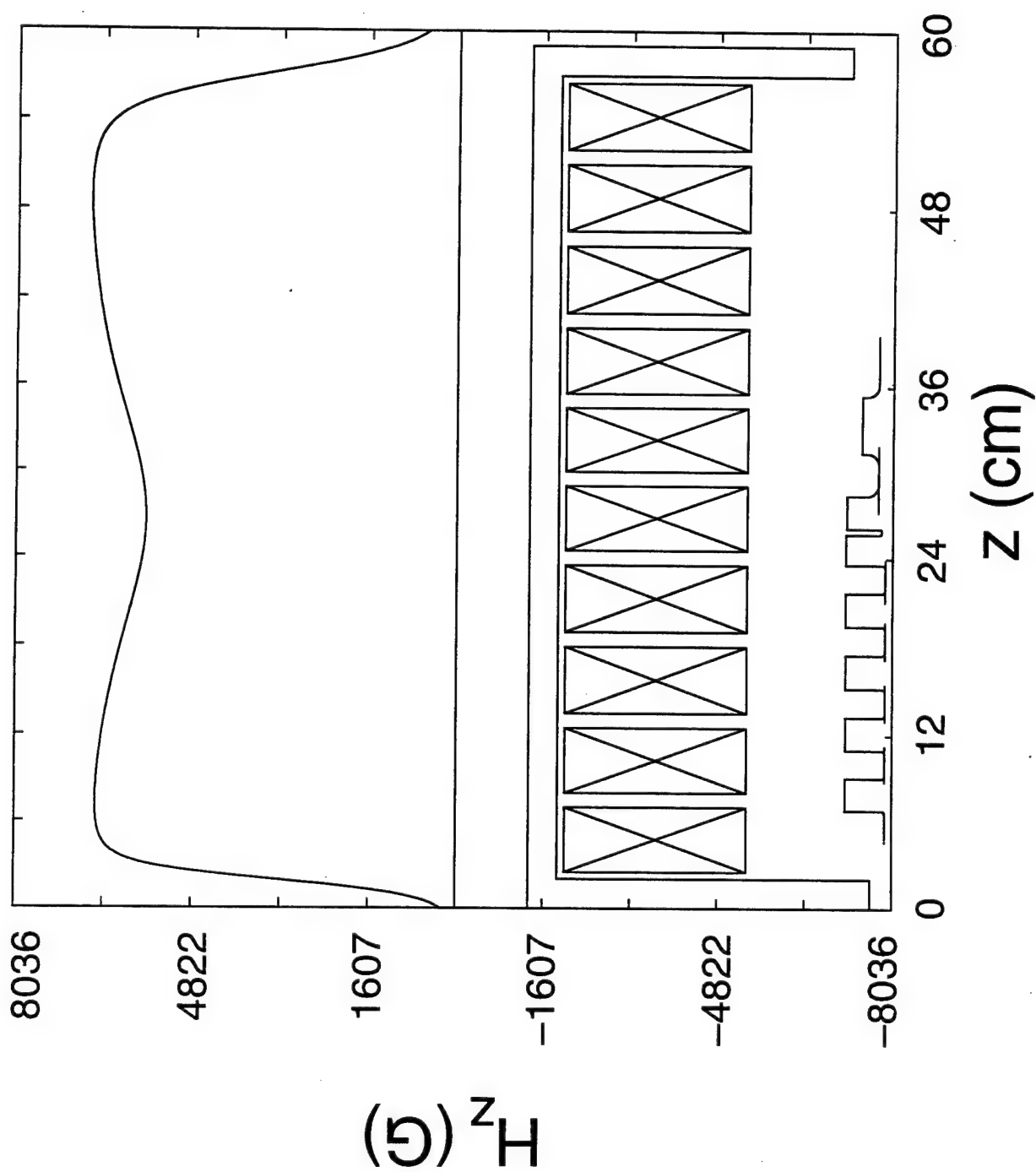
Fig. 11. Cross section view of the magnicon circuit, the magnet coils, and the iron yoke. Also shown is the axial magnetic field along the axis of the magnicon.

Electron Gun Design
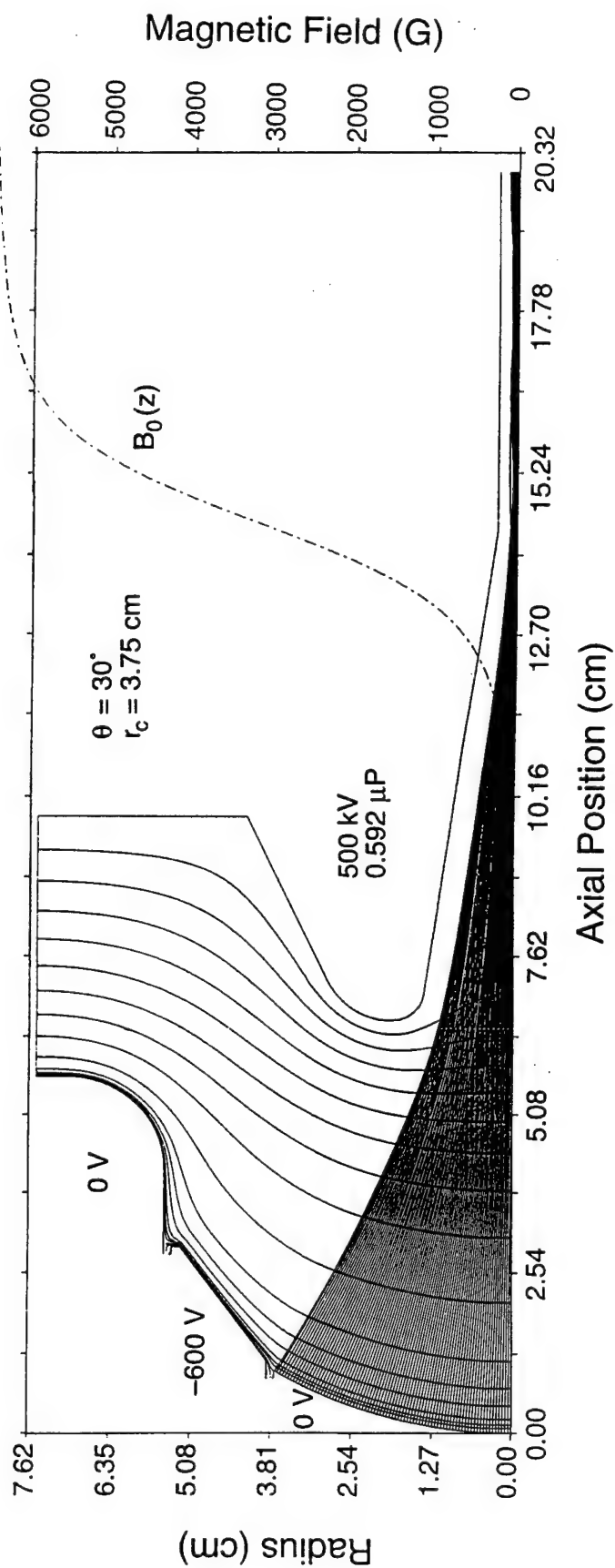
Fig. 12. Simulation of the preliminary design for the high convergence 500 kV, 200A magnicon electron gun, showing the electrode geometry and the electron trajectories.
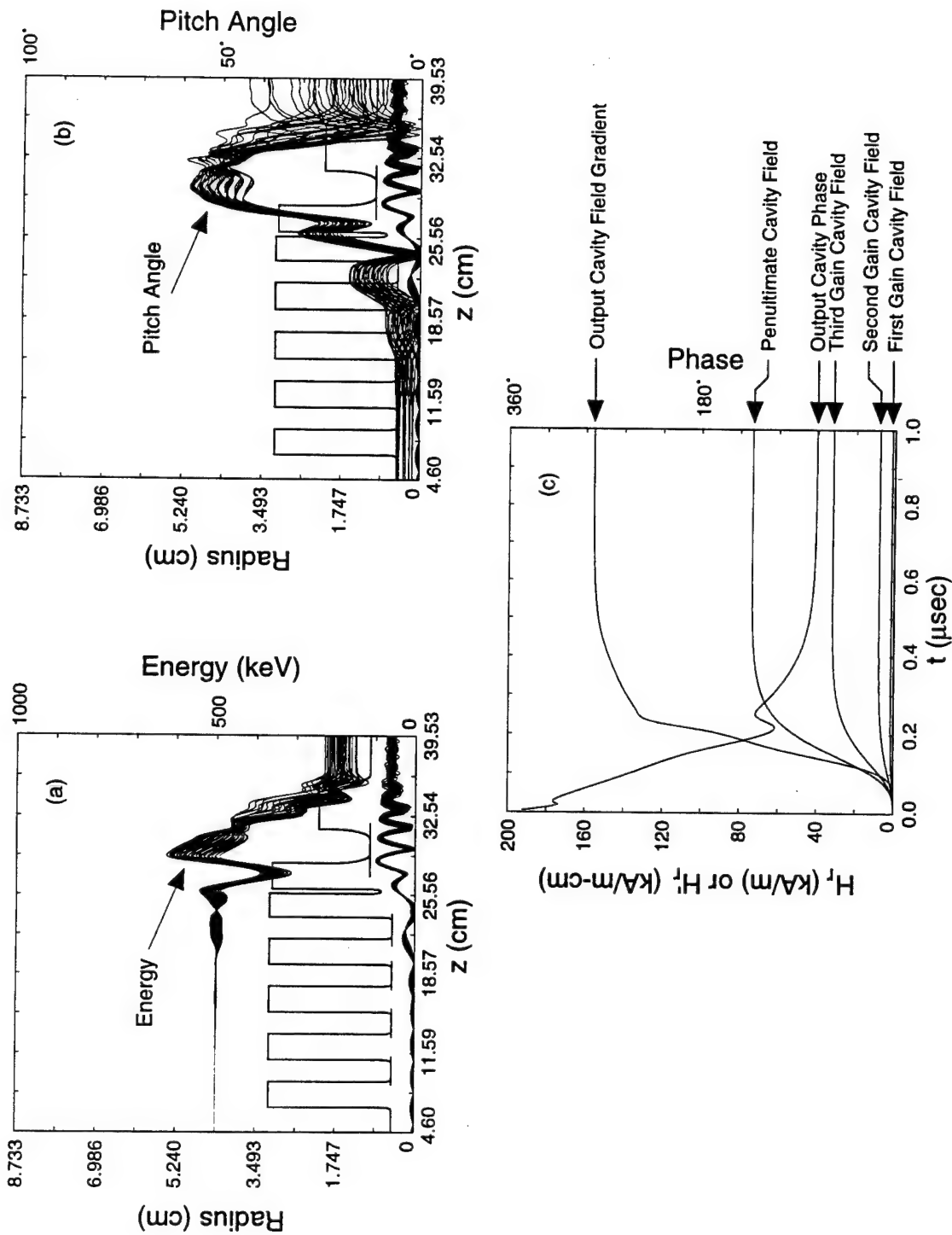
Fig. 13. Steady-state and time-dependent simulations of the final magnicon design for a 2.0-mm-diameter beam: (a) Steady-state simulation, showing the electron trajectories and energy versus z; (b) Steady-state simulation, showing the electron trajectories and pitch angles versus z; (c) Time-dependent simulation, showing the amplitudes of the on-axis fields in the three gain cavities and the penultimate cavity (kAm^{-1}), the gradient of the on-axis rf field in the output cavity (kAm^{-1}cm^{-1}), and the rf phase in the output cavity (0–360°).
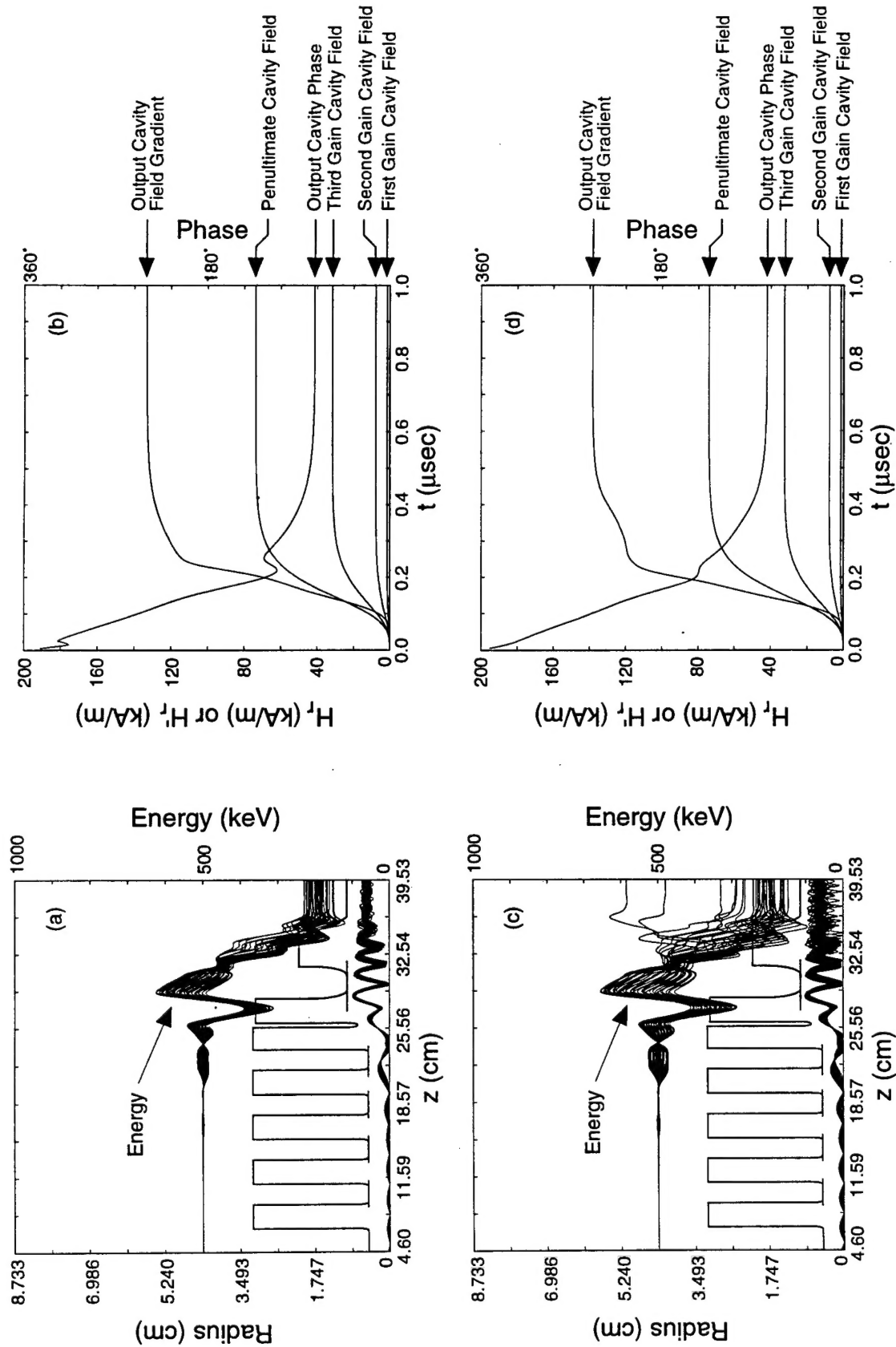
38

Fig. 14. Simulations of the final magnicon design for 1.5 and 2.5-mm-diameter beams: (a) Steady state simulation for a 1.5-mm-diameter beam, showing electron trajectories and energy versus z; (b) The corresponding time-dependent simulation, showing the amplitudes of the on-axis fields in the three gain cavities and the penultimate cavity (kAm^{-1}), the gradient of the on-axis rf field in the output cavity [kAm^{-1} cm^{-1}], and the rf phase in the output cavity (0–360°). (c,d) Steady-state and time-dependent simulations for a 2.5-mm-diameter beam.
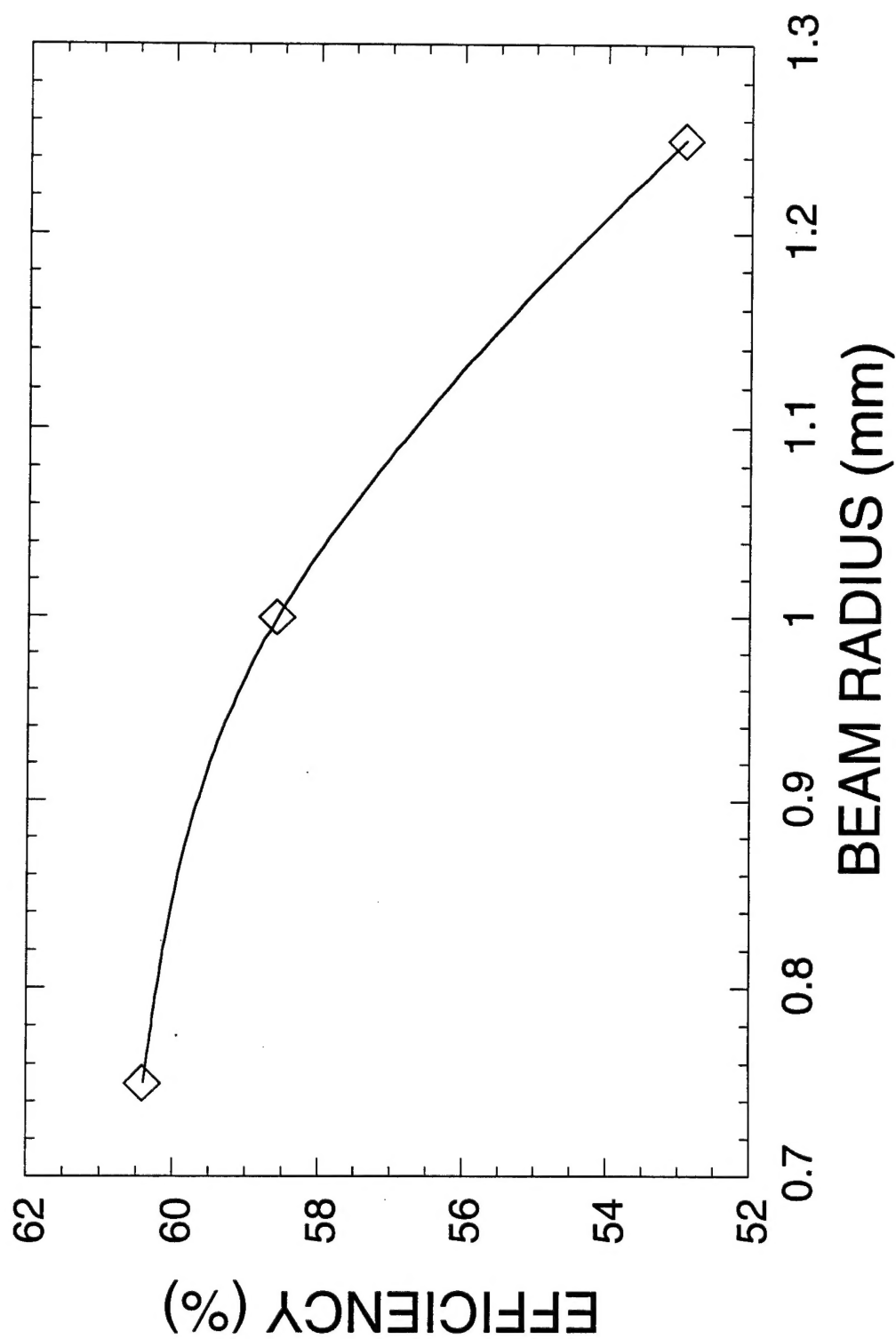
39

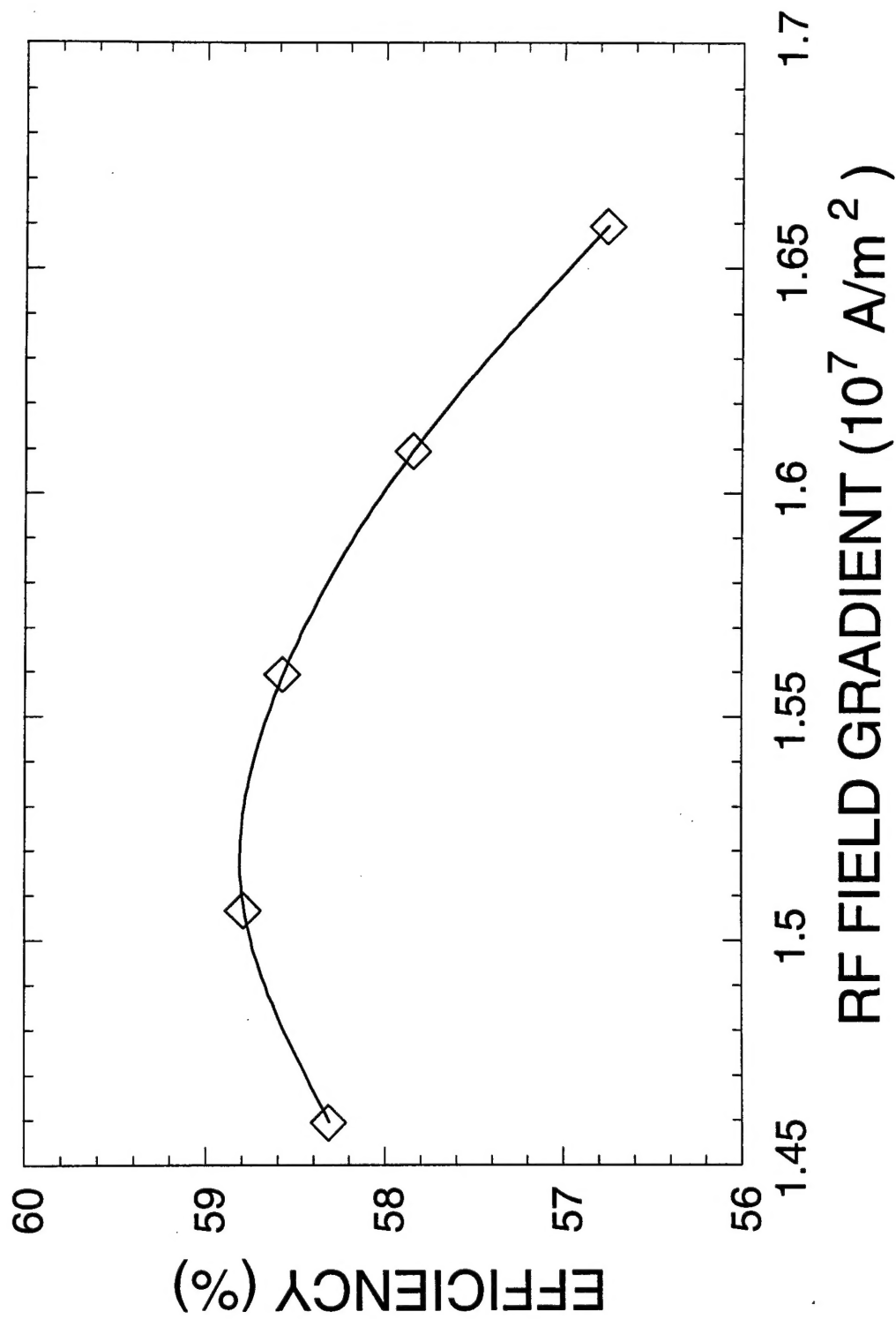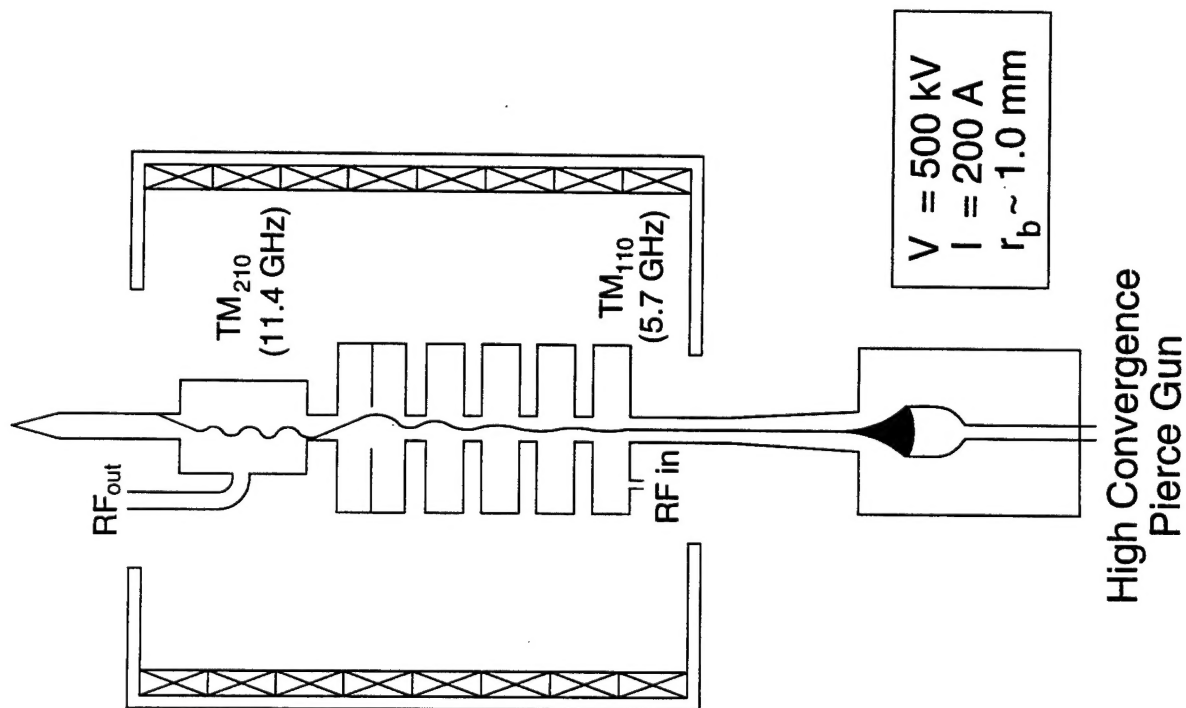Fig. 15. Efficiency vs beam radius for the final magnicon design

Fig. 16. Efficiency vs transverse rf magnetic field gradient in the output cavity for the final magnicon design.

Frequency	11.424 GHz
Power	58 MW
Pulse width	1.5 µsec
Repetition rate	10 pps
Efficiency	58 %
Drive frequency	5.7 GHz
Gain	57 dB

TM$_{210}$ (11.4 GHz)

TM$_{110}$ (5.7 GHz)

RF$_{out}$

RF in

V = 500 kV
I = 200 A
r$_b$ ~ 1.0 mm

High Convergence Pierce Gun

Fig. 17. Schematic of high efficiency frequency-doubling magnicon amplifier